Paper:
Krüger, C., Lisitsin-Baranovsky, E., Ofer, O., Turgeon, P., Vermette, J., Ayotte, P. & Alexandrowicz, G. (2018). A magnetically focused molecular beam source for deposition of spin-polarised molecular surface layers. *The Journal of Chemical Physics, 149*(16), 164201
http://dx.doi.org/10.1063/1.5048521

A magnetically-focused molecular beam source for deposition of spin-polarised molecular surface layers.

C. Krüger,[1] **E. Lisitsin-Baranovsky**,[1] **O. Ofer**,[1] **P-A. Turgeon**,[2]
J. Vermette,[2] **P. Ayotte**,[2] and **G. Alexandrowicz**[1,3,*]

[1]***Schulich Faculty of Chemistry,***
Technion - Israel Institute of Technology,
Technion City, Haifa 32000, Israel.
[2]***Département de Chimie, Université de Sherbrooke,***
2500 Boulevard Université, Sherbrooke, Québec, Canada J1K 2R1
[3]***Department of Chemistry, Swansea University,***
Singleton Park, Swansea SA2 8PP, United Kingdom.

(Dated: October 7, 2018)

Abstract

Separating molecular spin isomers is a challanging task, with potential applications in various fields ranging from astrochemistry to magnetic resonance imaging. A new promissing method for spin-isomer separation is magnetic focusing, a method which was shown to be capable of producing a molecular beam of ortho-water. Here, we present results from a modified magnetic focusing apparatus and show that it can be used to separate the spin isomers of acetylene and methane. From the measured focused profiles of the molecular beams and a numerical simulation analysis we provide estimations for the spin purity and the significantly improved molecular flux obtained with the new setup. Finally, we discuss the spin-relaxation conditions which will be needed to apply this new source for measuring NMR signals of single surface layer.

The nuclear magnetic moment (nuclear spin) is a general property of atoms. The different combinations in which atomic spin states can be added up, lead to different possible values of the total nuclear spin state of a molecule, I, known as molecular spin-isomers. While the energy splitting associated directly with the nuclear spin is typically very small ($0.17\,\mu$eV for protons in a 1 T magnetic field), the total nuclear spin state also determines, through symmetry properties, the allowed rotational states which have much higher energies. As a result, molecular spin-isomers may have signficantly different physical properties[1]. The separation of the spin isomers of molecular hydrogen, ortho ($I = 1$) and para ($I = 0$) H_2 is rather straight forward and has been established almost a century ago[2], consequently many applications have been developed which exploit the different physical properties of these two isomers. In contrast, it is quite difficult to separate the spin isomers of other molecules. Optical methods have been successfully used to produce small deviations from the equilibrium populations (e.g. [3, 4] and others). Separation, based on selctive adsorption has also been reported[5], however, attempts to reproduce or explain these experiments were unsuccessful, raising doubts about the interpretation of these experiments[6–8]. A few years ago, a new approach to spin isomer separation, based on magnetic focussing was applied to a molecular beam of water, resulting in a very high purity ortho-H_2O beam[9]. Further experiments showed that the focused ortho-molecules can be stored in a cold isolation matrix for hours before converting into para-H_2O[10]. A few years later, separation of the H_2O isomers using electric field deflection was also demonstrated[11]. While the molecular beam flux in the electric field deflection experiments was even lower than that achieved with magnetic focusing, this approach added the novel possibility of isolating para-H_2O molecules. In a recent set of experiments, the electrical deflection method was applied to study spin-isomer selective chemical reactions[12]. Both the magnetic and electric spin isomer separation techniques mentioned above are essentially beam deflection experiments inspired by pioneering work of Stern, Gerlach, Estermann and others [13, 14]. Magnetic and electric beam deflection has also been successfully applied to study the stereodynamics of gas phase reactions [15–18]. Various motivations exist for further developing these new spin-isomer separation techniques and extending them to a larger variety of molecules. One reason to develop separation techniques is for studying nuclear spin conversion rates, especially in the context of astrophysics and astrochemistry. The relative populations of spin-isomers are extracted from spectroscopic measurements of the interstellar media in space, due to the extremely

slow conversion between different spin-isomers in rare-field conditions, these relative populations have been used to infere the formation temperature of the molecule in the far past[19]. However, the interpretation of the astrophysical measurements relies on assumptions regarding the mechanisms of nuclear spin conversion, assumptions that have been questioned by recent experimental studies[20]. The ability to separate spin isomers of various molecules in the lab will enhance our understanding of nuclear spin conversion and contribute to the open questions in this field. Another potentially important application of spin separation is enhancing the sensitivity of nuclear magnetic resonance (NMR) experiments [21]. NMR is one of the most common techniques to study the microscopic structure, chemical nature and dynamics of materials. It is commonly used in chemistry, material sciences, medicine and many other fields. While this technique has many advantages it also suffers from one particularly signficant drawback, it is typically limited to samples which include a large number of molecules due to its limited sensitivity. This restriction arises from the fact that the signal in an NMR experiment is proportional to the net magnetization or spin polarisation, i.e. the difference between the populations of the different spin states. The small Zeeman energy splitting induced by the magnetic field leads to Boltzman factors which are painfully close to one, and consequently typical polarisations of a few tens of ppm are achieved. Thus, to obtain a signal equivalent to that of one molecule, a sample with $\approx 10^5$ molecules is needed. While this restriction has not stopped NMR from being a widely-used technique it has severly limited its application in particular research fields. One of those is surface science, where surface layers often contain only 10^{14} particles, well under the detection limit for conventional NMR. Various techniques are being developed to try and tackle the sensitivity issue and significant progress has been made over the years [22], nevertheless, NMR is still not generally applicable to surface layers. In this paper, we describe a magnetic focusing apparatus which was designed to provide a relatively high flux of spin selected molecules. The apparatus is part of an ongoing attempt in our group to perform NMR of surface layers. We will show results for the performance of this setup, in terms of magnetic focussing and flux for two molecules, acetylene and methane, and discuss the implications of this study to achieving the ambitious goal of measuring NMR from a single surface layer.

The magnetically focused beam source used in this study is a modification of the deflection setup used to perform the first magnetic separation of ortho and para H_2O[9]. The modifications include improved pumping of the source chamber and a longer hexapole

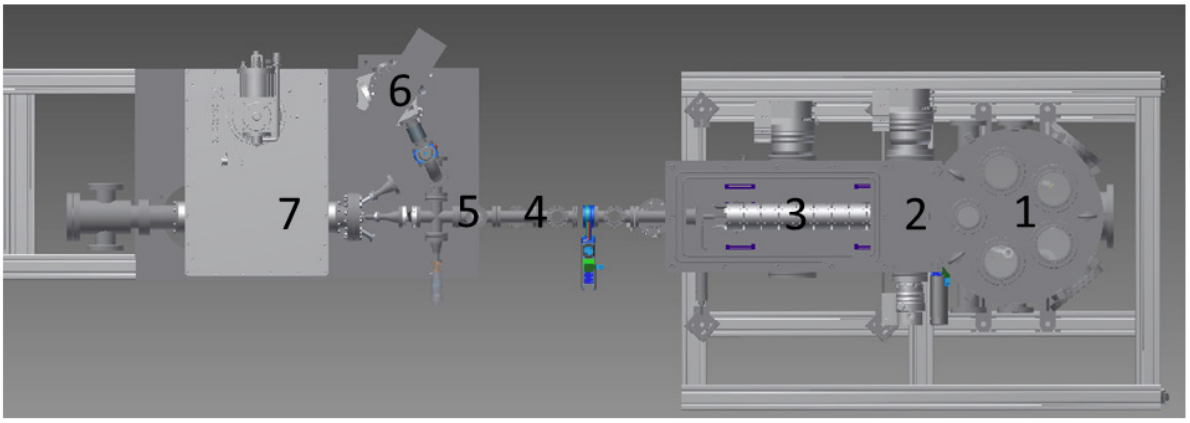

FIG. 1. Schematic of the experimental setup which includes a (1) supersonic molecular beam source, (2) skimmer and differential pumping stages, (3) magnetic hexapole assembly, (4) extractor ion gauge, (5) horizontal and vertical scanning apertures and (6) a quadrupole mass spectrometer. The beam line ends at the surface of a cold substrate unto which the beam particles adsorb. The substrate is located within the horizontal bore of a super conducting magnet (7), which will be used for future NMR experiments.

magnet resulting in an improved molecular beam flux while maintaining a sufficiently high purity of the separated spin-isomer. Figure 1 shows a schematic of the setup and labels the main components relevant to the experiments presented in this paper. A supersonic beam is formed in the source chamber (1) by expanding a gas (or a mixture of gasses) through a temperature controlled 150 µm nozzle. The propagating beam goes through a 500 µm skimmer (2) and two further differential pumping stages before entering the chamber which houses the focusing hexapole magnet (3). The hexapole magnet is built from 9 hexapole magnet elements following the basic design introduced by Jardine et al. [23]. The magnetic field leads to a Zeeman splitting of the quantized energy levels, which depends on the projection of the spin along the quantization axis, I_z. The field within the hexapole is strongly inhomogeneous with a radial gradient proportional to the distance from the beam axis, resulting in quantized radial forces. More specifically, low field seeking particles ($I_z < 0$) are pushed inwards (focused), high field seeking particles ($I_z > 0$) are pushed outwards (defocused) and particles with a vanishing spin projection ($I_z = 0$) are unaffected by the magnetic fields and continue moving along their original straight line trajectories[24]. Further down the beam line we located two scanning flags (5), one containing horizontal slits and one containing

vertical slits. Using these two flags allows us to define a square aperture through which the beam can continue to propagate and block any beam trajectories which do not fit within the aperture. The aperture can be moved in space vertically and horizontally with a precision better than 0.01 mm. We note that while the magnetic focusing method enhances the relative population of the focused species down the beam line with respect to the other species, a certain fraction of the unfocused species will remain close to the beam axis and arrive at the target. For applications where this is a problem, further filtering can be achieved using a beam block [15].

In order to obtain the spatial profile of the molecular beam we use the following scheme. Particles which miss the aperture lead to an increase in the pressure of the vacuum chamber surrounding the flags, this increase is measured using both an extractor ion gauge (Leybold IE514) (4) which records the total pressure and a mass spectrometer (6) used to differentiate the contributions of different species when using gas mixtures in our molecular beam (Hiden HAL301/PIC). Beam particles which pass through the aperture continue towards a separate chamber where they adsorb unto a cold surface, and hence do not contribute to the pressure rise in the ion gauge and mass spectrometer. Figure 2 shows an example of the experimental raw data measured for a beam mixture of argon and acetylene. The plot shows the mass spectrometer count rate as function of time measured while scanning the position of a 2×2 mm square aperture. The black circles and blue crosses show the count rate for a mass of 20 amu and 26 amu respectively, following the partial pressures of argon (doubly ionised) and acetylene. For clarity figure 2 shows the doubly ionised argon peak which produces a count rate more comparable to that of acetylene, however, in all other results presented in this paper the main peak of argon (40 amu) was followed.

In order to convert raw data of the type shown in figure 2 to the profile of the beam we followed the following post processing: (1) The count rate, measured with the beam completely blocked, was subtracted from the scan. (2) The result was inverted (minimal pressure rise = maximal beam intensity passing through the aperture). (3) The temporal scan was converted to the aperture position by synchronising the aperture motion and measured count rate. (4) The profile was normalized and centered. (5) The data was converted to molecular flux using the estimated pumping speed[25] and the calculated partial pressures (calibrated using the total pressure measured by the ion gauge and the relative count rates of the different mass component measured by mass spectrometer, considering

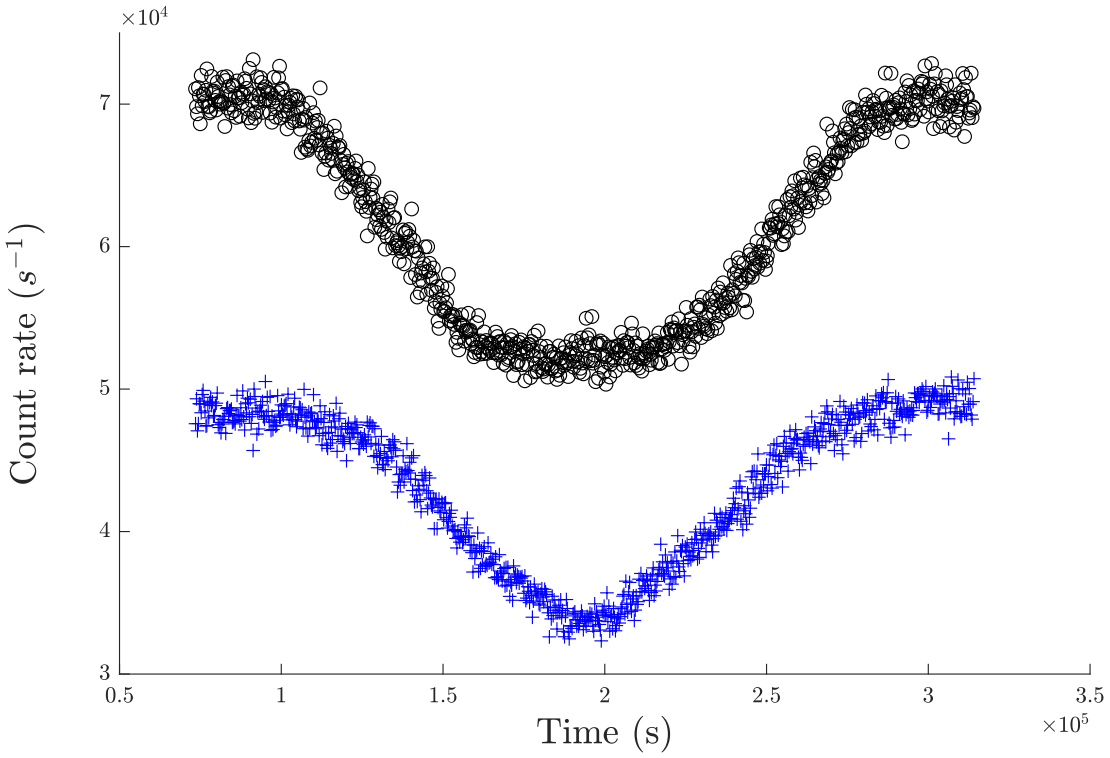

FIG. 2. An example of the raw experimental data used to extract the beam profiles. The black circles and the blue crosses show the mass spectrometer count rate of argon and acetylene measured while scanning the horizontal position of a $2 \times 2\,\mathrm{mm}$ aperture. Since the motion of the flag was synchronised with the mass spectrometer measurements, the time profile can be converted into a spatial profile.

the Ion gauge correction factors [26] as well as the relative sensitivity factors for the mass spectrometer).

To assess our ability to magnetically focus and spin separate different molecular species, we measured the profiles of beams of acetylene (C_2H_2) and methane (CH_4), mixed in heavier carrier gasses (argon and neon). Mixing the molecules with carrier gasses serves two main aims. The heavier atoms of the carrier gasses, when they are the majority gas, slow down the molecules (inverse seeding) [27], and make it possible to magnetically deflect the molecules and focus one spin isomer. The carrier gasses we used are non-magnetic and are not affected by the magnetic lens, hence they provide a useful comparison to the molecular profiles. The unfocused profiles also allow us to verify the geometry of the setup (source size, aperture

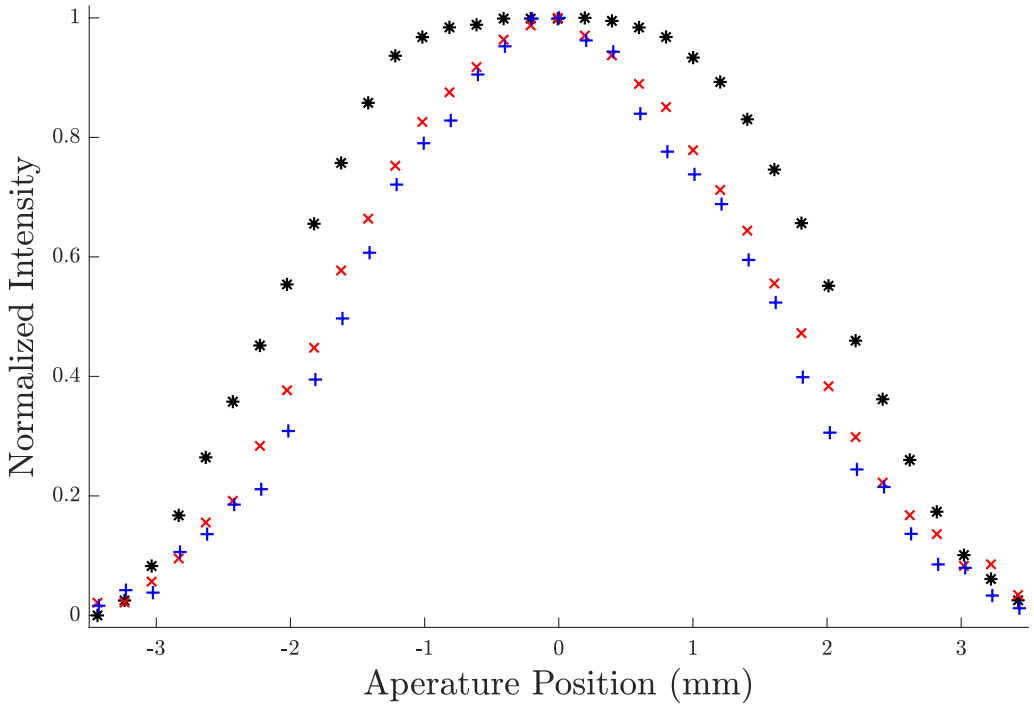

FIG. 3. Acetylene/argon beam profiles for dilution ratios of 1/3 (red x marker), 1/10 (blue cross marker) respectively ($P_{nozzle} = 150\,\text{mbar}$). It can be seen that Acetylene molecules are focused better at lower concentrations, however, the differences between the different dilution ratios are relatively small compared with the difference between the profiles of argon atoms (black star marker) and acetylene molecules.

diameters and aperture positions), a geometry that is used when we employ numerical simulations to analyse our results.

The nuclear spins of the protons in an acetylene molecule can couple to produce the triplet of ortho-acetylene states ,$I = 1$, with spin projections of $I_z = 1, 0, -1$ or para acetylene $I = 0, I_z = 0$. The hexapole we use focuses low-field seeking states, hence the $I_z = -1$ state is focused, the $I_z = 1$ is defocused and the two $I_z = 0$ states are unaffected by the magnetic fields (i.e. they maintain their original straight line trajectories). Since both the defocused state and the non-magnetic states ($I_z = 0$) eventually diverge from the beam line axis, after a long enough flight path we expect the focused species to dominate the region surrounding the beam axis, this is the basic principle of the magnetic separation approach. Figure 3 shows the (normalized) beam profiles measured for molecular beams with different

C_2H_2/Ar mixing ratios. The black stars show the profile of the argon atoms which are unaffected by the magnetic field gradients in the hexapole. The shape of the argon profile represents the geometry of the system, i.e. the possible straight line trajectories which start at the source and reach the scanning aperture position without hitting the fixed apertures (or the hexapole magnet walls) along the flight path. The blue cross markers show the profile of the C_2H_2 molecules in an experiment where the molecules were mixed in an argon beam with a partial pressure ratio $P_{C_2H_2}/P_{Ar} = 1/10$. Under sufficiently diluted conditions the minority species (C_2H_2) is expected to adopt the relatively slow velocity of the majority species (argon)[27] , $V = \sqrt{\frac{C_p T_N}{m_{Ar}}} = 556\,\mathrm{m\,s^{-1}}$, where $T_N = 25\,^{\circ}\mathrm{C}$ is the nozzle temperature, C_p is the heat capacity and m_{Ar} the mass of argon atoms. The fact that the molecular profile is significantly narrower than that of the carrier gas tells us that the magnetic focusing is working and we have a high content of the focused species. Another qualitative observation which we can make, is that increasing the C_2H_2 content of the beam (red x markers) widens the profiles, i.e. reduces the focusing power of the magnetic lens. This trend can be expected as high concentrations of the minority gas are expected to lead to velocity slips[27], i.e. the average velocity of the two species in the binary mixture deviates, the lighter molecules move with a higher velocity and consequently are not efficiently focused. The motivation behind increasing the C_2H_2 concentrations is related to the overall higher molecular flux which can be achieved this way (see Figure 4), however, it is clear that this increase in flux comes at the expense of the spin purity. It is important to note that while the data in figure 4 allows us to compare the relative molecular flux of different dilution ratios, the absolute flux estimations contain a relatively large error ($\pm 25\%$) related mostly to uncertainties in the absolute ion gauge pressure readings and sensitivity correction factors.

Methane is a more complex quantum mechanical system. The 4 protons can couple to produce the meta, ortho and para spin isomers ($I = 2, 1, 0$). Similarly, to the case of C_2H_2 discussed above, the molecules will be either focused, defocused or unaffected by the hexapole depending on their spin projections. In contrast to C_2H_2, we also have states with $I_z = -2, +2$ which experience stronger focusing and defocusing forces. It is also important to note that spin projections of $|I_z| < 2$ are obtained for more than one total spin state. For applications requiring a high purity of a particular total spin value, this is a restriction. In contrast, for applications related directly to I_z, such as depositing a spin hyper-polarised layer, the goal is achieving a high net magnetisation of the layer regardless of the total spin

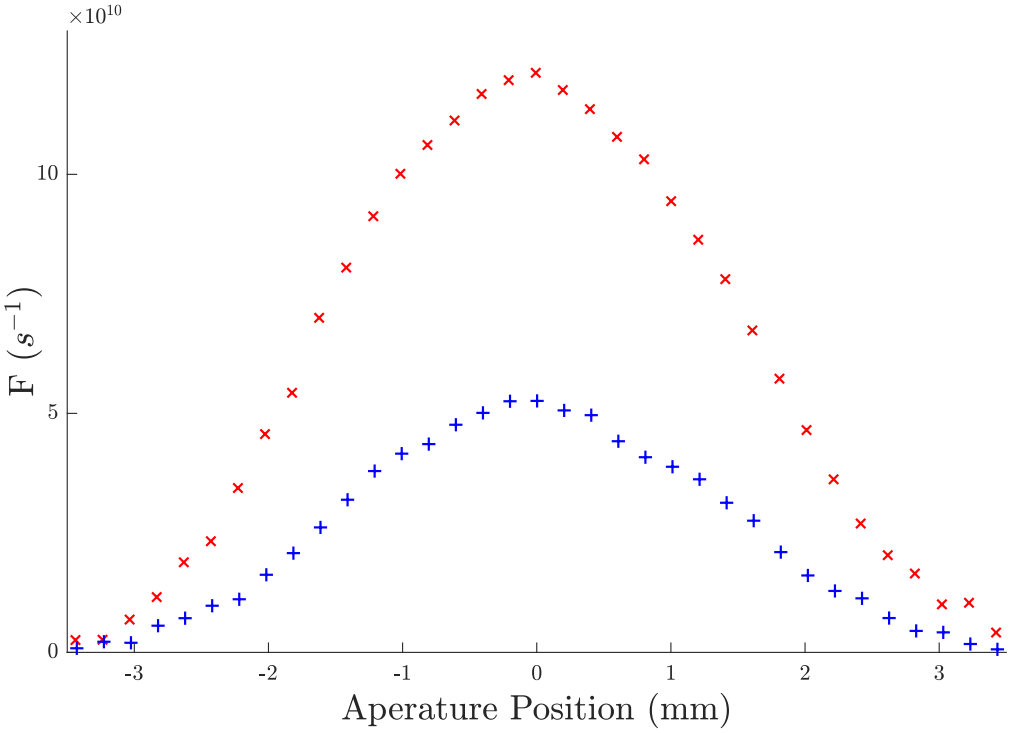

FIG. 4. Absolute flux profiles of acetylene/argon beams with dilution ratios of 1/3 (red x marker) and 1/10 (blue cross marker) respectively (P_{nozzle} = 150 mbar).The absolute flux, $F(\mathrm{s}^{-1})$, is the molecular beam flux integrated over the area of a 2mm x 2mm aperture.

or symmetry of the state in the gas phase.

Figure 5 shows the experimental normalized profiles measured for mixed CH_4/Ne beams. Neon was chosen as a carrier gas, since the lighter mass of methane and the stronger focusing requires a faster molecular velocity. The black circles show the profile of the carrier gas, whereas the blue crosses show the profile of CH_4 in a highly diluted mixture. The significantly narrower profile of the molecular species indicates that indeed we are capable of magnetically focusing the beam, and that it's composition will be biased in favor of the low-field seeking states. Similarly to the case of C_2H_2, increasing the molecular concentration in the binary gas mixture (red x and blue cross markers) widens the beam, however, even when we use pure methane (purple stars), the beam is still significantly focussed with respect to a non-magnetic species. Thus, if the object is to deliver a high flux of molecules with sufficiently large average magnetisation, high concentration beams and even pure methane beams might be useful, an issue we discuss later. Figure 6 compares the absolute flux profiles

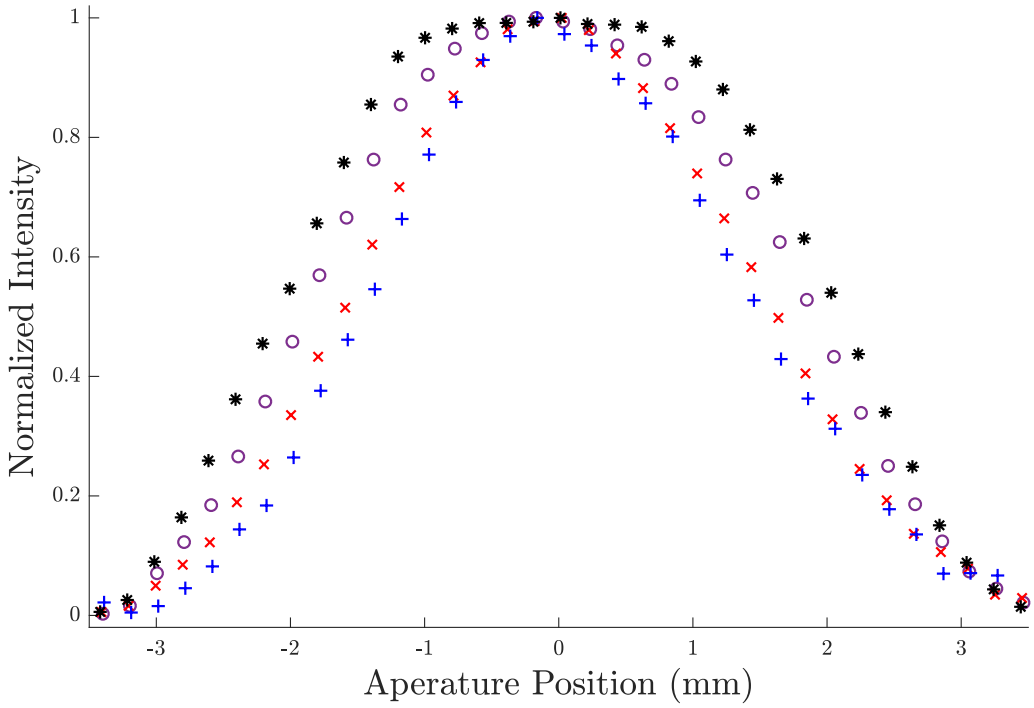

FIG. 5. Focusing of different Methane concentrations in Neon (black star marker). The profiles shown are at dilution ratios of 1/9 (blue crosses) and 1/3 (red x marker) as well as pure methane (purple circles). All experiments were done at $P_{nozzle} = 150\,\text{mbar}$.

of the different concentrations.

Figures 3 - 6 show clear differences between the measured profiles of the molecular species and the carrier gasses. While these differences tell us that the magnetic focusing and consequently the spin isomer separation technique is working, further analysis is needed to quantify the separation purity and the corresponding spin flux which can be used for deposition of hyper polarised layers. In order to analyze the results we used a numerical calculation which simulates the trajectories of the beam particles through the apparatus.

The semi-classical approach we use follows the trajectories classically, where the quantum nature is reflected in the quantization of the magnetic moment direction which is aligned either parallel or anti-parallel to the local direction of the magnetic field. Due to the cylindrical symmetry of the beam line geometry, it is only the radial forces within the hexapole magnet which can focus or defocus the trajectories and change the probability of passing through the setup. The simulation includes the following stages. The initial starting points

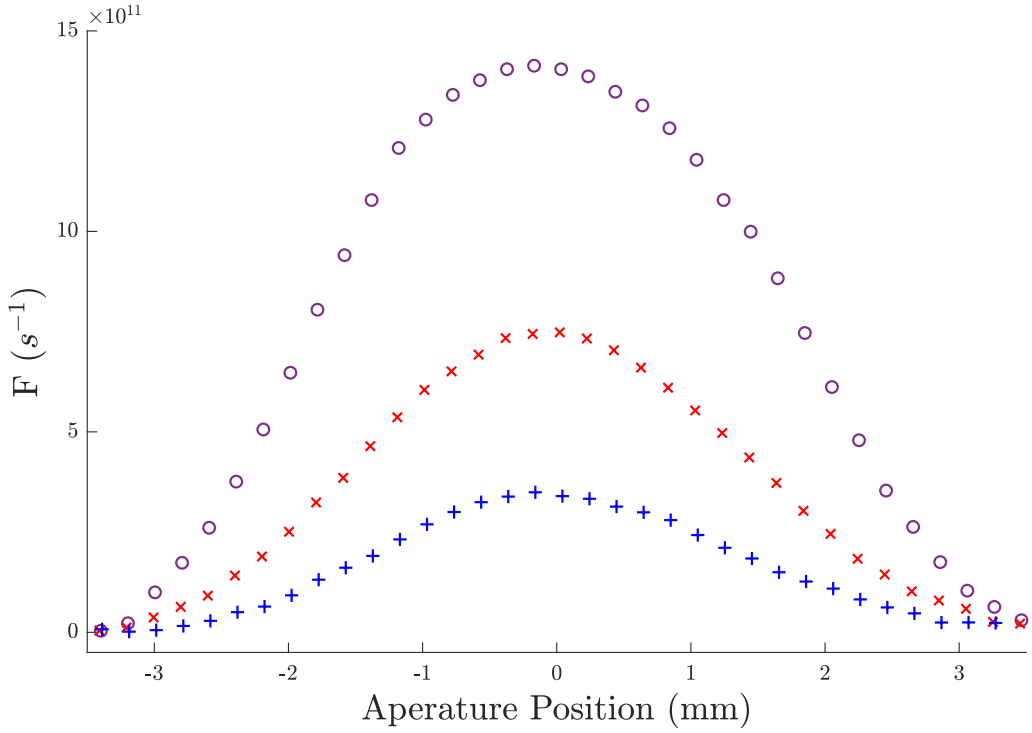

FIG. 6. Methane/Neon beam profile with $P_{nozzle} = 150\,\text{mbar}$ and concentrations 1/9, 1/3 and pure respectively (the markers correspond to figure 5). Here the absolute fluxes of the different species are represented with regard to the scanning aperture position.

are chosen from a uniform distribution of coordinates within the beam source. To account for the finite energy distribution in the experiment, the velocities were chosen from a normal distribution with a standard deviation of 20 %, centred around the velocity of the carrier gas atoms in an ideal supersonic expansion. The azimuthal and polar starting angles are chosen from random distributions, the azimuthal angle ranges uniformly from 0 to π whereas the polar angle is chosen within $-\phi_{max}$ to ϕ_{max} where ϕ_{max} is the maximal angle that a particle, starting at the source, can enter the hexapole.[28] The trajectories of the emitted particles are then followed through the hexapole elements where they experience magnetic forces and through the field free regions where they move in straight lines. An ideal hexapole field equation is used to calculate the trajectories within the magnetic elements, previous studies have shown that the higher order poles which can be extracted from a finite element analysis have a very subtle effect on the trajectories[23]. A fourth order Runge-Kutta algorithm is used to calculate the trajectories within the magnetic elements. Particles which hit the

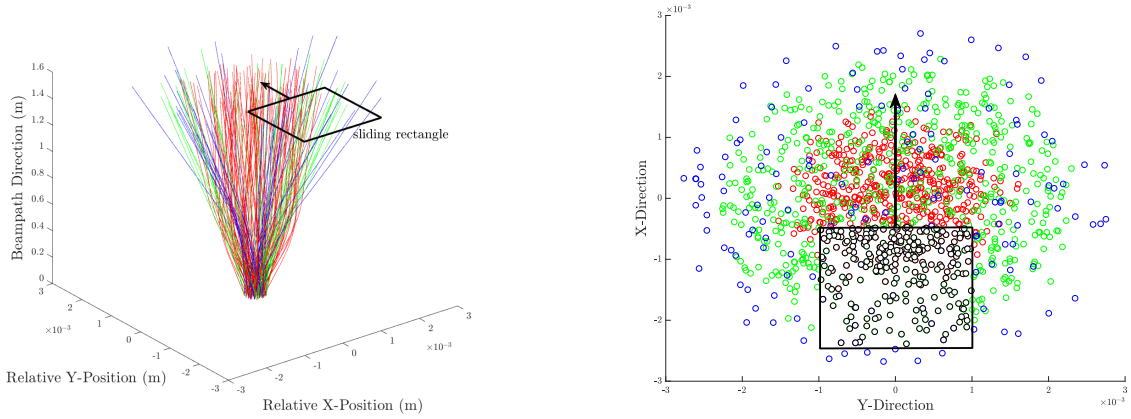

(a)Trajectory calculation for different spin projections.

(b)2-D cut at measurement position.

FIG. 7. An illustration of the simulated trajectories of the different spin isomers of acetylene. The left panel shows the trajectories of focused, unfocused and defocused species, plotted using red, green and blue lines respectively. The right panel shows the positions of the particles within the plane where the scanning apertures are located (using the same color coding). The black circles mark the particles which make it through the rectangular aperture. To avoid clutter only a fraction of the calculated trajectories are represented.

hexapole wall, or the fixed apertures located along the beam line are omitted, leaving us with only the beam particles which reach the scanning aperture region. Finally, the calculations described above are performed for each of the spin states in the molecular beam mixture and the results of the different calculations are summed according to the expected statistical weight to produce a simulated beam profile. Figure 7(a) shows the simulated trajectories of acetylene molecules with different spin isomers $I_z = 1$ (blue), 0 (green) and -1 (red). Once the trajectories are calculated for all the different spin isomers, the simulated profile is generated by counting all the trajectories which pass through a 2×2 mm rectangle at the position of the scanning aperture (Z = 1.6 m). Each data point corresponds to the normalized number of particles going through the rectangle, the centre of which reflects the scaning aperture position (see figure 7(b)). In order to produce a realistic simulation, the relative initial spin populations need to be taken into account. For example, for acetylene molecules, there are two $I_z = 0$ states ($I = 1$ and $I = 0$) and only one $I_z = 1$ or $I_z = -1$ states.

Figure 8 presents the simulated acetylene and argon profiles on top of the experimental results (normalized profiles). We start by noting that the simulated profile of the carrier gas (argon in this case) plotted as a dashed line fits the measurement quite well. The similarity of these two profiles reassures us that the geometry (aperture diameters and positions) used in the simulation closely resembles that of the experimental setup. The black dashed and dotted line represents the simulated result for acetylene using the simulation conditions detailed above. As we expect, this curve is more focused than the non-magnetic carrier gas, however, the curve is narrower than the experimental profile we measured for acetylene. A very similar situation is encountered in the case of methane presented in figure 9, where the simulated profile for methane is narrower than the most narrow experimental profile (1/9 dilution).

The comparison with the simulation shows that the focusing properties of the experimental setup deviate from the nominally expected behavior. There are two obvious beam properties which could lead to a broadened profile of the focused molecular beam, a wider energy distribution or a faster average velocity. We start with examining the effect of the width of the velocity distribution. The velocity distribution in supersonic beams has a complex dependency on many parameters such as the nozzle and skimmer shape, diameter and temperature, nozzle-skimmer distance and the composition of the seeded beam. Since our setup does not allow a direct measurement of the velocity distribution, there is an uncertainty in the width of this distribution. Figure 10 shows the simulated profiles of acetylene beams with various widths. While increasing the velocity distribution width leads to a broadening of the profile, even if we use unrealistically wide velocity distributions the corresponding broadening of the focused profile is much too small to explain the experimental width. Consequently, we conclude that the velocity distribution width does not contribute significantly to the width of the experimental profile. Another phenomenon which takes place in seeded supersonic beams is velocity slips[27]. When the concentration of the minority species is too high the velocity of these particles will be different from that of the majority species. Since in our case, the minority species is both lighter and has molecular degrees of freedom (larger C_P) we expect the minority species to move faster than the nominal speed of the carrier gas, when its concentration is relatively high. Figure 11 shows that velocity slip can indeed explain the broadened experimental profiles. The experimental results for methane/neon beams with dilution ratios of 1/9, 1/3 can be reproduced quite nicely using

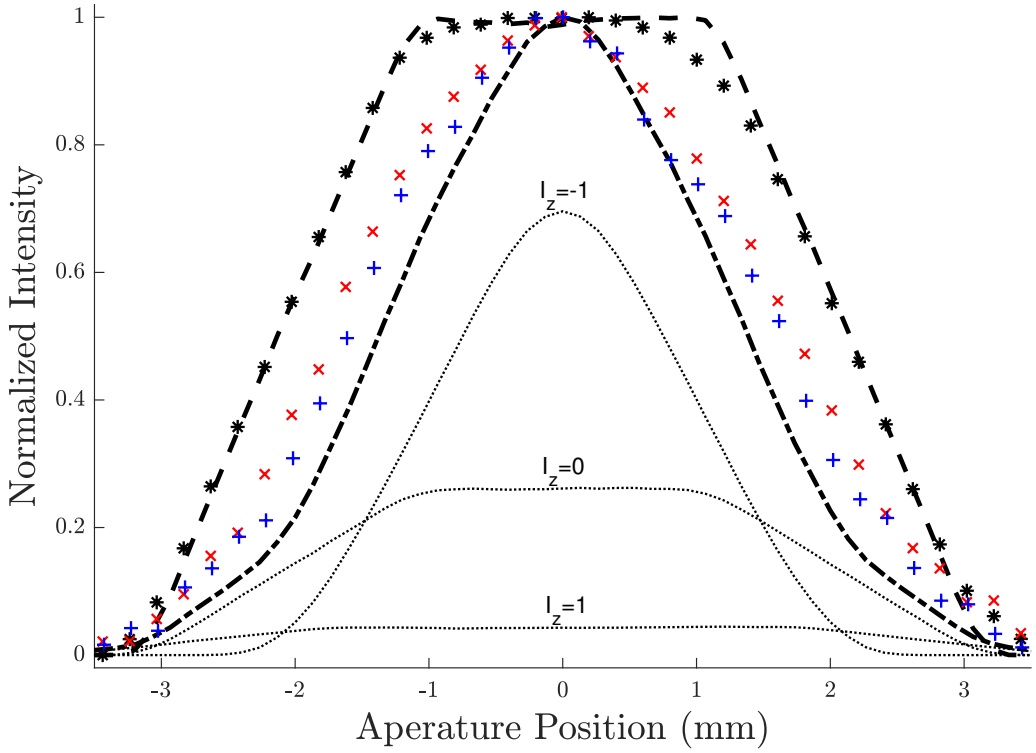

FIG. 8. Comparison of experimental and simulated profiles for acetylene / argon beams. The experimental data at different dilution ratios is plotted using the same color coding as in figure 3. The dashed line and dashed-dotted lines are the simulated profiles for argon and acetylene respectively. The 3 thin dotted lines show the different I_z contributions which make up the simulated acetylene profile.

simulations with mean velocities which are 18 and 25 percent higher than the neon velocity (dashed blue and dotted red lines). To fit the pure methane profile an even higher velocity is needed. The full purple line shows a simulation with $1.45V_{neon}$which is almost as wide as the experimental profile. Similarly, the width of the acetylene profiles is best reproduced when assuming velocity slips of 18% and 10% for acetylene/argon ratios of 1/3 and 1/10. It is important to note that an even higher velocity $1.6V_{neon}$ fits the pure methane data slightly better, however, a value of $1.45V_{neon}$ represents an upper limit for what we think the velocity could actually be. A velocity of $1.45V_{neon}$ is consistent with the heat capacity of methane at room temperature, $C_P = 36\,\mathrm{J\,mol^{-1}\,K^{-1}}$[29], however, it is an upper limit estimate since the rotational temperature, and correspondingly the heat capacity, are likely

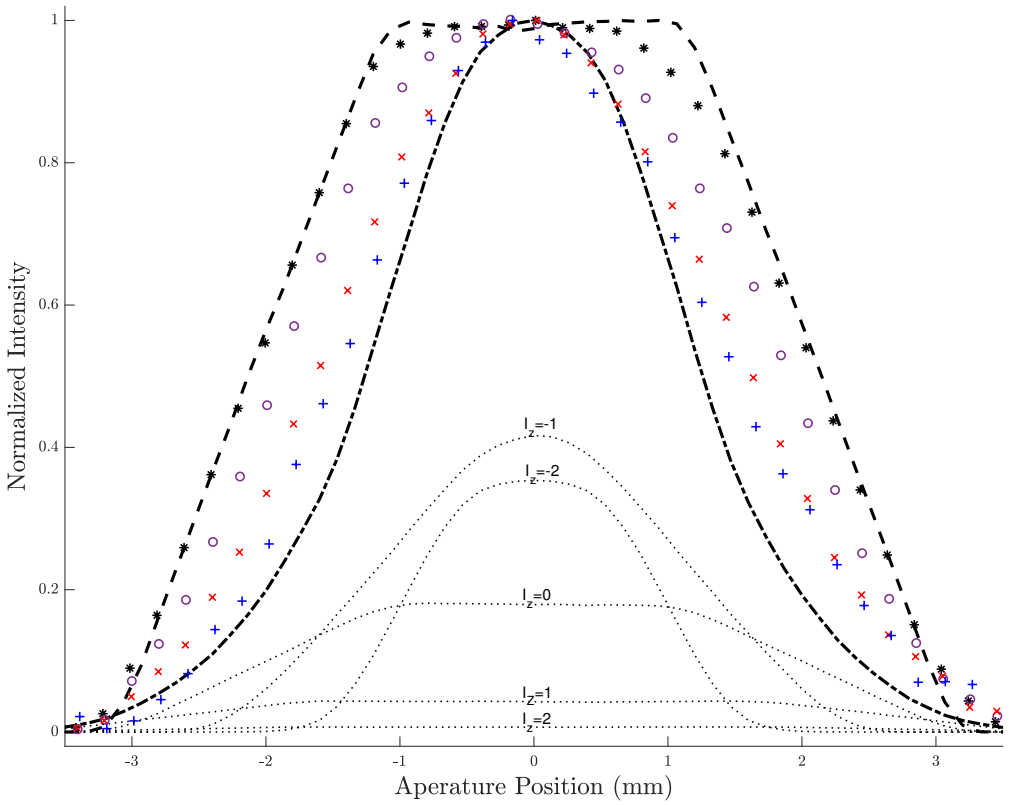

FIG. 9. Comparison of experimental and simulated profiles for methane /neon beams. The experimental data at different dillution ratios is plotted using the same color coding as in figure 5. The dashed line and dashed-dotted lines are the simulated profiles for neon and methane respectively. The 5 thin dotted lines show the different I_z contributions which make up the simulated methane profile. Note that even though $I_z = -2$ produces the narrowest distribution, the $I_z = -1$ contribution is the most dominant contribution. This is due to a competing effect between the focusing effect and the relative population (for example both I=1 and I=2 include a $I_z = -1$ projection.

to be lower after expanding through the nozzle.

It is important to highlight other scenarios which could alter the beam profile. In particular, the experimental curves can be fitted by the simulation if we allow different initial populations of the spin states in the supersonic expansion. However, we are not aware of any physical justification for such deviations from the expected equilibrium populations and did not further pursue this option. Another complexity which was ignored in our simple

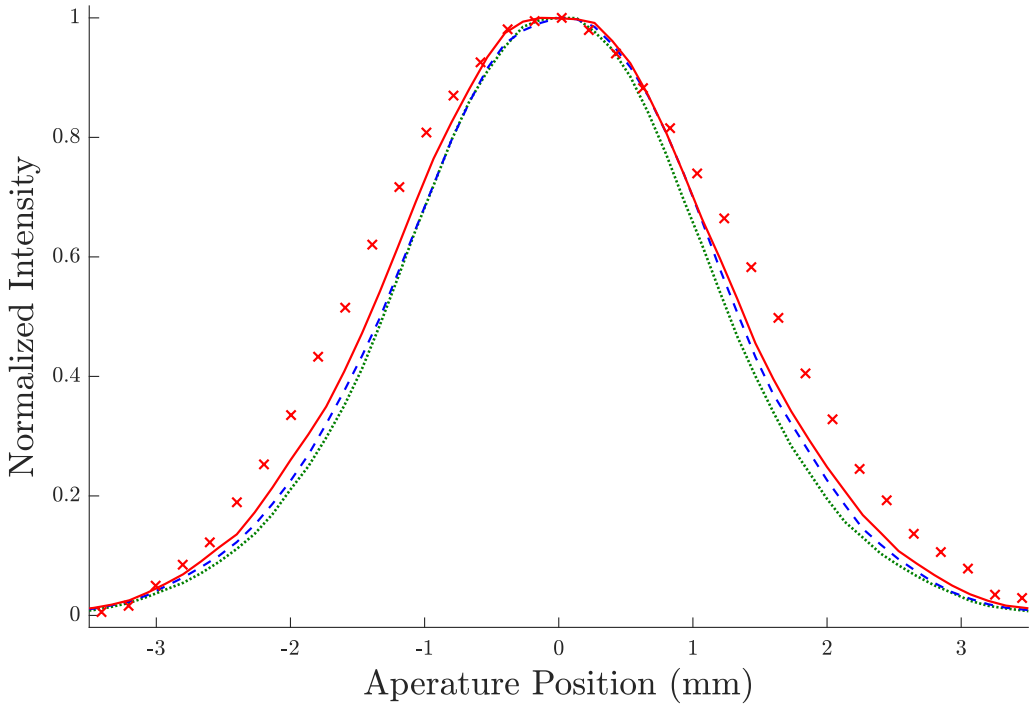

FIG. 10. Comparison of the experimental methane profile (red x marker, dillution ratio 1/3) and simulated profiles with velocity distribution widths of 40 (green dotted line), 60 (blue dashed line) respectively 80 % (red line) of the average velocity.

treatment is the effect of the magnetic forces on different rotational projection states. To take these into account one would need to determine the rotational temperature of the beam and the population of the rotational states, solve the Ramsey Hamiltonian for each total spin species (similar to what was done for H_2[30]), obtain the magnetic field dependence of the multiple eigenstates and include these in the numerical simulation. While such work is beyond the scope of this publication, the fact that typically the rotational magnetic moments are substantially weaker than the nuclear magnetic moments, suggests that taking the rotational deflections into account would not substantially change the focusing profiles. Furthermore, since the rotational temperature is expected to be very sensitive to the mixing temperatures, the relatively small changes of the measured profiles suggest that the rotationally induced broadening is not the dominant mechanism.

The fact that we can mimic the experimental profile of the beam when we allow for velocity slips, allows us to estimate the average spin projection of the beam particles which pass

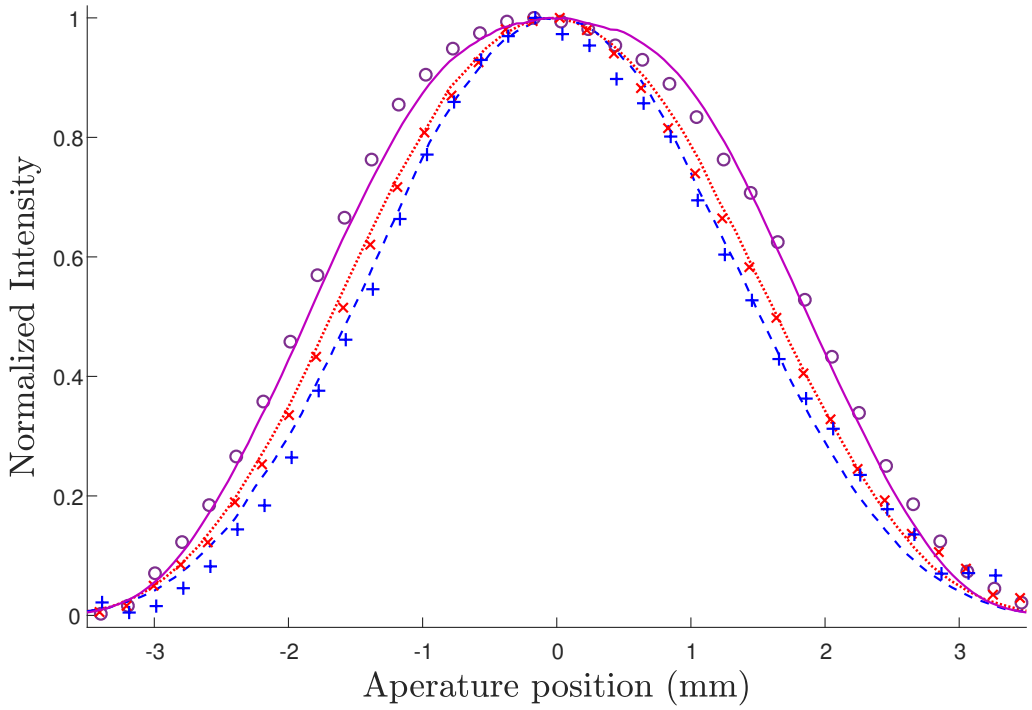

FIG. 11. Comparison of the experimental methane profiles of different dilution ratios, pure, 1/3 and 1/9 (using the same markers and colors as in figure 5) with simulated profiles of different velocities: $1.45V_{neon}$ (purple full line), $1.25V_{neon}$ (red dotted line) and $1.18V_{neon}$ (blue dashed line) times the velocity of neon.

through the aperture and could be used as a hyperpolarized spin deposition source. Table I shows the overall molecular flux (through the 2mm x 2mm aperture), F, the molecular beam velocity which produces the best fit to the experimental profile, v'_{best}, the average spin projection, $\langle I_z \rangle$, and the estimated flux of polarized protons, $F_P = 2F\langle I_z \rangle$ for each type of molecular beam.

There are a few insights which can be gained from table I. First, while the focusing is not perfect it is capable of producing extremely high average spin projections and seems like a very promising source for hyperpolarized deposition of surface layers. For comparison, the equilibrium average spin projection at room temperature and a magnetic field of 1T is only a couple of parts per million. A second insight is that even though less diluted beams have a lower average spin projection (probably due to enhanced velocity slip), this is compensated by the higher flux achievable and delivers a higher number of polarized protons to the

Beam	F $[10^{12}\frac{molecules}{second}]$	v'_{best} $[\frac{m}{s}]$	$\langle I_z \rangle$ $[\frac{spins}{molecules}]$	F_P $[10^{12}\frac{spins}{second}]$
C_2H_2 1:3	0.1	$1.18v_{Ar}$	-0.5	0.1
C_2H_2 1:10	0.05	$1.10v_{Ar}$	-0.6	0.06
CH_4 pure	1.4	$1.45v_{Ne}$	-0.6	1.7
CH_4 1:3	0.7	$1.25v_{Ne}$	-0.8	1.2
CH_4 1:9	0.3	$1.18v_{Ne}$	-0.9	0.6

TABLE I. Estimations for the polarized proton flux obtained by fitting the different molecular beams experiments with the numerical simulation and allowing for a velocity slip of the molecular species in the binary mixture.

target, in particular the highest flux of polarized protons is achieved with a pure methane beam. Finally, since the number of adsorption sites on a 2mm x 2mm patch is on the order of $5 \cdot 10^{13}$ or less, a hyperpolarized mono-layer of methane can be deposited within about 30 seconds, whereas longer times are needed for mixed methane/neon beams and the various acetylene/argon beams we tried. If one wishes to use these beams to accumulate a hyperpolarized molecular surface layer and perform a NMR experiment on this layer, spin-lattice relaxation times of minutes to tens of minutes will be required to preserve the spin polarization and produce a strong enough NMR signal.

While the comparisons shown in table I provide a very useful guide for choosing the molecular beam composition and designing future NMR experiments, some care should be taken when using the values of the absolute flux of polarized proton due to several uncertainties. In particular, we estimate that the accuracy of the ion gauge and the use of general gas correction factors for electron bombardment ionisation, introduce a total uncertainty in the absolute flux of up to $\pm 25\%$. Furthermore, since our system does not allow for direct measurements of the velocity distributions, we can not rule out the existence of other significant contributions to the broadening of the focusing profile, other than the velocity slip in the binary gas mixture. If such contributions are dominant, the actual velocity slip might be smaller and the simulated profiles need to be recalculated to determine more accurate estimations of $\langle I_z \rangle$. A further consideration, when using this molecular beam setup for future NMR experiments is avoiding unwanted I_z transitions along the beam line. While the hexapole magnet was designed to maintain adiabatic conditions within this region,

transitions can occur between the hexapole magnet and the deposition target due to either fast changes in the local magnetic field or due to spin rotation coupling. Consequently, strong enough holding fields (in the range of $10^1 - 10^2$ gauss) need to be used to ensure that the Zeeman terms in the Hamiltonian are larger than the coupling terms [30].

Summary and conclusions

We have presented experimentally measured profiles of molecular beams of acetylene and methane which were passed through a hexapole magnet. In both cases, the molecular species is focused with respect to the inert carrier gas demonstrating that significant spin separation of these molecules has been successfully achieved. The experimental broadenings can be reproduced by numerical simulations when 10% to 25% velocity slips of the molecular species within the binary mixtures are assumed. The ability to reproduce the focused profiles with the numerical simulation allows us to calculate the average spin projection and provide estimations for the flux of polarized protons which the setup can deliver. The extreme hyperpolarization of the magnetically focused beam is approximately 5 orders of magnitude higher than the typical polarization in standard NMR experiments. The flux estimations, which reach values of up to $1.7 \cdot 10^{12}$ polarized spins per second, allow us to determine the condition which will be required to perform NMR measurement of a deposited layer of methane / acetylene, namely, the spin relaxation rates of the deposited surface layers should be slow with respect to the required deposition times, estimated as minutes to a few tens of minutes depending on the molecular beam composition.

ACKNOWLEDGEMENTS

G.A. is grateful to Prof. Malcolm Levitt for his helpful comments. This work was funded by the European Research Council under the European Unions seventh framework program (FP/2007-2013)/ERC grant 307267, the Horizon 2020 research and innovation program - grant 772228 and the Israel Science Foundation (grant 755/16).

* ga232@technion.ac.il

[1] H. Haken and H. C. Wolf, *Molecular Physics and Elements of Quantum Chemistry* (Springer-Verlag Berlin Heidelberg, 2004).

[2] A. Farkas, Science **81**, 517 (1935).

[3] Z.-D. Sun, K. Takagi, and F. Matsushima, Science **310**, 1938 (2005).

[4] B. Nagels, M. Schuurman, P. Chapovsky, and L. Hermans, Physical Review A **54**, 2050 (1996).

[5] V. I. Tikhonov and A. A. Volkov, Science **296**, 2363 (2002).

[6] H.-H. Limbach, G. Buntkowsky, J. Matthes, S. Gründemann, T. Pery, B. Walaszek, and B. Chaudret, ChemPhysChem **7**, 551 (2006).

[7] S. Veber, E. Bagryanskaya, and P. Chapovsky, J. Exp. Theo. Phys. **102**, 76 (2006).

[8] P. Cacciani, J. Cosleou, and M. Khelkhal, Phys. Rev. A. **85** (2012), 10.1103/PhysRevA.85.012521.

[9] T. Kravchuk, M. Reznikov, P. Tichonov, N. Avidor, Y. Meir, A. Bekkerman, and G. Alexandrowicz, Science **331**, 319 (2011).

[10] P.-A. Turgeon, P. Ayotte, E. Lisitsin, Y. Meir, T. Kravchuk, and G. Alexandrowicz, Phys. Rev. A **86**, 062710 (2012).

[11] A. Horke, Y.-P. Chang, K. Dlugolecki, and J. Kupper, Angewandte Chemie International Edition **53**, 11965 (2014).

[12] A. Kilaj, H. Gao, D. Rösch, U. Rivero, J. Küpper, and S. Willitsch, Nature Communications **9**, 2096 (2018).

[13] W. Gerlach and O. Stern, Zeitschrift für Physik **9**, 349 (1922).

[14] I. Estermann and O. Stern, Zeitschrift für Physik A Hadrons and Nuclei **61**, 95 (1930).

[15] P. R. Brooks, E. M. Jones, and K. Smith, The Journal of Chemical Physics **51**, 3073 (1969).

[16] D. Watanabe, H. Ohoyama, T. Matsumura, and T. Kasai, Phys. Rev. Lett. **99**, 043201 (2007).

[17] J. Zou, S. D. S. Gordon, S. Tanteri, and A. Osterwalder, The Journal of Chemical Physics **148**, 164310 (2018).

[18] S. D. S. Gordon, J. Zou, S. Tanteri, J. Jankunas, and A. Osterwalder, Phys. Rev. Lett. **119**, 053001 (2017).

[19] M. Mumma, H. Weaver, and H. Larson, Astronomy and Astrophysics **187**, 419 (1987).

[20] T. Hama, A. Kouchi, and N. Watanabe, Science **351**, 65 (2016).

[21] M. H. Levitt, *Spin Dynamics: Basics of Nuclear Magnetic Resonance* (Wiley, 2008).

[22] M. E. Halse, TrAC Trends in Analytical Chemistry **83**, 76 (2016).

[23] A. P. Jardine, P. Fouquet, J. Ellis, and W. Allison, Review of Scientific Instruments **72**, 3834 (2001).

[24] S. Y. T. van de Meerakker, H. L. Bethlem, N. Vanhaecke, and G. Meijer, Chemical Reviews **112**, 4828 (2012).

[25] A. Chambers, *Basic Vacuum Technology* (CRC Press, 1998).

[26] F. Nakao, Vacuum **25**, 431 (1975).

[27] G. Scoles, D. Bassi, U. Buck, D. Laine, and C. Braun, Applied Optics **28**, 3258 (1989).

[28] Note that the polar angle distribution needs to be non-uniform (the probability should increase linearly with ϕ) to achieve an equal distribution in space of trajectories emitted from the source.

[29] G. J. Vogt and K. S. Pitzer, The Journal of Chemical Thermodynamics **8**, 1011 (1976).

[30] N. F. Ramsey, Phys. Rev. **85**, 60 (1952).